

# Radial-Grating Pendulum-Structured Triboelectric Nanogenerator for Energy Harvesting and Tilting-Angle Sensing

Chuan He, Bao Dong Chen, Tao Jiang, Liang Xu, Chang Bao Han, Guang Qin Gu, and Zhong Lin Wang\*

A radial-grating pendulum-structured triboelectric nanogenerator (RP-TENG) is demonstrated for energy harvesting and tilting-angle sensing. By employing the pendulum structure, the RP-TENG is applied to capture biomechanical energy from human motion or harness the energy in acceleration or deceleration processes of moving vehicles. The electrical performance of the RP-TENG is systematically studied by simulating the repetitive movement of human arms and legs during walking at different repetition frequency. At the resonance frequency of 1.5 Hz, the open-circuit voltage ( $V_{OC}$ ) and short-circuit current ( $I_{SC}$ ) produced are  $83.6 \pm 0.5$  V and  $8.46 \pm 0.08$   $\mu$ A, respectively, and the maximum instantaneous power density is  $35.2$  mW  $m^{-2}$  at a load resistance of 10 M $\Omega$ . Through parallel-connecting 4 pairs of triboelectric layers, the  $I_{SC}$  can be increased from 4.45  $\mu$ A for one pair of triboelectric layers to 12.83  $\mu$ A. Furthermore, owing to its high sensitivity to minor changes from the vertical level (the lower detection limit of the RP-TENG is 0.25°), a RP-TENG integrated tilt sensing alarm system is developed, which can be applied in security or seismic monitoring systems.

## 1. Introduction

Over the past few years, triboelectric nanogenerator (TENG) has been rapidly developed as energy harvesters and sensors.<sup>[1,2]</sup> Coupling triboelectric effect and electrostatic induction, TENG can directly convert irregular, small-scale mechanical energy into electricity.<sup>[3]</sup> Utilizing two triboelectric materials of different affinities for electrons, the TENGs can efficiently harvest energy from mechanical motions, or sense mechanical agitations through contacting-separating<sup>[4–6]</sup> or sliding between the two materials.<sup>[7,8]</sup> The contact mode of the TENG has been proven to be effective in harvesting energy of human walking<sup>[4]</sup>

and vibration.<sup>[5,6]</sup> The electrical output of the TENGs in the contact mode can be largely increased through surface modification<sup>[9,10]</sup> or structural optimization.<sup>[11,12]</sup> For the sliding mode, the output performance of the TENGs has also been greatly enhanced through advanced structural designs.<sup>[13–19]</sup> For example, by employing the grating structure, the TENG has a multiplied in-plane charge separation cycles, thus deliver an elevated output current.<sup>[7]</sup> In this regard, linear grating structure has been thoroughly studied for practical applications.<sup>[17,18]</sup> Furthermore, radial grating structures have also been presented for harvesting various rotatory energy and can be used as a practical power source for consumer electronics.<sup>[15,19]</sup> Besides energy harvesting, TENG has also been widely applied as self-powered sensors due to its excellent performance.<sup>[1]</sup> Based on the contact mode,

the TENG has been used as tactile sensors<sup>[20,21]</sup> and pressure sensor.<sup>[22]</sup> The sliding mode TENGs are able to track the magnitude and direction of 1D and 2D motions,<sup>[23]</sup> and sense displacement/speed with nanometer resolution and long detecting range using microgratings.<sup>[24]</sup>

In this article, we demonstrate a radial-grating pendulum-structured TENG (RP-TENG) for energy harvesting and tilting-angle sensing. Taking advantage of its pendulum structure, the RP-TENG has a quick response to external mechanical agitations, such as vibration, acceleration, and tilt motion. Thus, the RP-TENG can be applied to capture biomechanical energy from human motion, or harness energy in the acceleration or

Dr. C. He, Dr. B. D. Chen, Dr. T. Jiang, Dr. L. Xu, Dr. C. B. Han, G. Q. Gu, Prof. Z. L. Wang  
CAS Center for Excellence in Nanoscience  
Beijing Institute of Nanoenergy and Nanosystems  
Chinese Academy of Sciences  
Beijing 100083, P. R. China  
E-mail: zlwang@gatech.edu

Dr. C. He, Dr. B. D. Chen, Dr. T. Jiang, Dr. L. Xu, Dr. C. B. Han, G. Q. Gu, Prof. Z. L. Wang  
College of Nanoscience and Technology  
University of Chinese Academy of Sciences  
Beijing 100049, P. R. China  
G. Q. Gu  
University of Chinese Academy of Sciences  
Beijing 100049, China  
Prof. Z. L. Wang  
School of Materials Science and Engineering  
Georgia Institute of Technology  
Atlanta, GA 30332-0245, USA

 The ORCID identification number(s) for the author(s) of this article can be found under <https://doi.org/10.1002/admt.201700251>.

DOI: 10.1002/admt.201700251

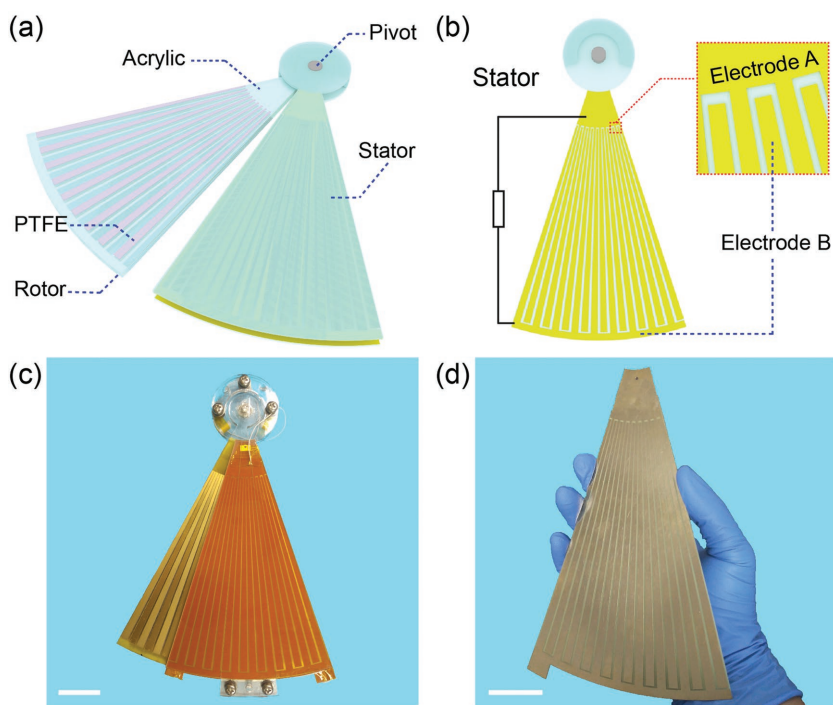


**Figure 1.** a) Schematic illustration of the RP-TENG. b) Schematic illustration of the stator. The inset is the enlarged view of interlocking sectorial electrode. c) Photograph of the RP-TENG. The scale bar is 6 cm. d) Photograph of the interlocking sectorial electrode. The scale bar is 3 cm.

deceleration processes of moving vehicles. Additionally, the RP-TENG can be used to harvest energy from tilt motions, such as the motion of ocean waves, and the scalability of the RP-TENG has also been proved. Furthermore, due to its high sensitivity to minor changes from the vertical level, a RP-TENG integrated tilt sensing alarm system is developed, which can be used in home security or seismic monitoring.

## 2. Results and Discussion

A RP-TENG has a sectorial structure consisting of two coaxially aligned components: a rotor and a stator. Both the rotor and stator have a radius of 200 mm and a central angle of  $36^\circ$ . **Figure 1a** is the schematic illustration of the RP-TENG. The rotor is suspended from the pivot, and can swing back and forth when the RP-TENG is subjected to external forces. In order to overcome the friction between the rotor and stator, a sectorial acrylic with a thickness of 5 mm is used as the supporting substrate for the rotor. On each side of the acrylic substrate, there are nine radially aligned sectorial polytetrafluoroethylene (PTFE) films with a length of 143 mm and a central angle of  $1.5^\circ$ . For the stator, it contains two identical units that come into contact with the rotor. On the inner surface of each unit, there are two interlocking sectorial copper (Cu) electrode combs, as illustrated in **Figure 1b**, and the inset shows the enlarged view of the electrodes. It can be seen that there are 18 radially aligned sectorial electrode fingers, where each finger has the same shape as that of the PTFE films. The top and bottom electrode combs are named Electrode A and Electrode B, respectively. Here, the

PTFE film with a thickness of  $80\ \mu\text{m}$  serves as the electronegative triboelectric layers, while the Electrode A and Electrode B as both the electropositive triboelectric layers and the electrode. The amplitude of the rotor,  $\theta$ , is defined as the included angle between the bisectors of the rotor and stator. The photographs of the RP-TENG and interlocking electrode combs are exhibited in **Figure 1c,d**, respectively. The interlocking electrode is fabricated by the print circuit board (PCB) technology. The detailed description of the RP-TENG is presented in the Experimental Section.

The structural design of the RP-TENG allows the oscillation of the rotor around its equilibrium position, where the bisectors of the rotor and stator are aligned. The working principle of the PR-TENG is depicted in **Figure 2a**, where the cross-section view that perpendicular to the bisector of the stator is illustrated. As demonstrated previously, the RP-TENG has a sandwich structure that consists of two pairs of triboelectric layers. When the rotor at its equilibrium position, as illustrated in **Figure 2(i)**, the grated PTFE films are fully aligned with Electrode A. According to the triboelectric series,<sup>[1]</sup> the electrons will be transferred from the Electrode A to PTFE films as a result of the triboelectric effect.

Thus, the total amount of positive triboelectric charges on the Electrode A should be the same with the negative triboelectric charges. In this position, the positive and negative charges compensated with each other, hence there is no current flows between the Electrode A and Electrode B. When the rotor slides rightward, the grated PTFE film slides from the Electrode A to Electrode B, as presented in **Figure 2(ii)**, hence there is a potential drop that drives the positive charges flow from the Electrode A to Electrode B. Once the grated PTFE films overlap the Electrode B, all the positive charges are being transferred and another equilibrium being achieved (see **Figure 2(iii)**). As the rotor keeps moving rightward, the positive charge will transfer from the Electrode B to Electrode A, and induces a reverse transient current (see **Figure 2(iv)**) until the grated PTFE films are in full contact with the Electrode A again (**Figure 2(i)**). This is one cycle of generation process. Thus, as the rotor swings around the equilibrium position, the sliding motion between the rotor and stator produces an alternating current in the external circuit.

**Figure 2b,c** shows the open-circuit voltage ( $V_{OC}$ ) and short-circuit current ( $I_{SC}$ ) of the PR-TENG, respectively, where the rotor is released from the maximum displacement angle on the right side,  $\theta = \theta_{max} = 36^\circ$ , and the stator is vertically placed. At  $\theta_{max}$ , there is no overlap between the rotor and stator. When released, the rotor is subjected to a restoring force due to gravity and accelerates back to the equilibrium position, during which the contact area between the triboelectric layers increases. The increasing contact area leads to an increase in triboelectric charges, hence the  $V_{OC}$  and  $I_{SC}$  produced also increase. As the rotor passes the equilibrium position ( $\theta = 0$ ),

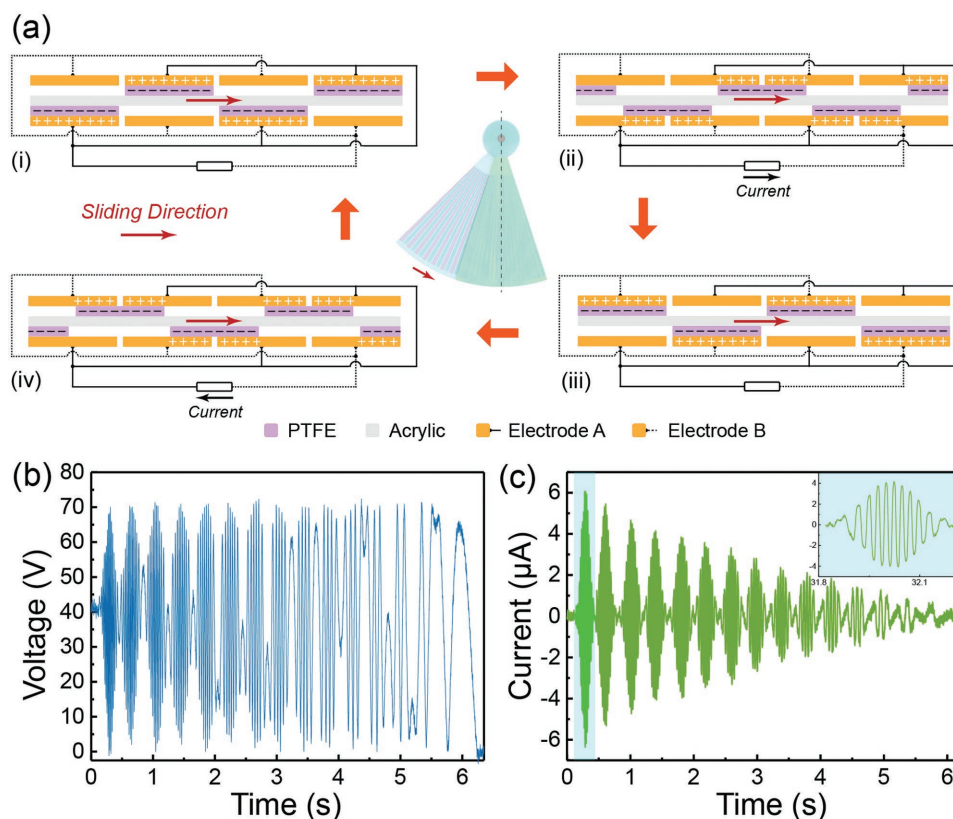


**Figure 2.** a) Working principle of the RP-TENG. b) Open-circuit voltage ( $V_{OC}$ ) and c) short-circuit current ( $I_{SC}$ ) of the PR-TENG that released from maximum displacement angle. The inset shows the enlarged view of highlighted region.

the  $V_{OC}$  and  $I_{SC}$  reach their peak value. Then the  $V_{OC}$  and  $I_{SC}$  decrease until the rotor reaches the largest displacement angle on the left side, where  $\theta < \theta_{max}$ . This process is half-cycle of the swing motion. The corresponding current produced in the first half-cycle is shown in the inset of Figure 2c. It can be seen that the signal first increases and then decreases, and the peak value occurs when the rotor passes the equilibrium position. As the rotor swing back and forth, the amplitude of the rotor continues to decline due to the friction, and we can see that it takes 15 half-cycles until the rotor eventually comes to rest, as shown in Figure 2b,c. In the meantime, the friction also slows down the motion of the rotor, thus increases the charge separation time and lengthens the duration of the peak signal. During the whole process, the peak value of the  $V_{OC}$  remains almost steady at  $70.9 \pm 0.8$  V, while the peak value of the  $I_{SC}$  generated in the first half cycle is  $6.10 \mu A$  and then decreases in the subsequent swings. The reason that the peak value of the  $V_{OC}$  does not decay over time can be attributed to the fact that the  $V_{OC}$  produced between the Electrode A and B reaches the maximum as the rotor slide from position (i) to (iii) (see Figure 2a), i.e.,  $\theta > 1.5^\circ$ , because of the grating structure.

Human motion is an important mechanical energy source that can be harvested by various generators.<sup>[1,25]</sup> Of these, the TENG has been proven to be an effective approach for harvesting different types of human motion energy, such as the energy of footfalls<sup>[11]</sup> and vibration during walking.<sup>[4]</sup> Besides, the swing motion of the arms and legs also constitutes a large

proportion of the mechanical energy from human motion.<sup>[26]</sup> In order to evaluate the electrical performance of the RP-TENG for harvesting the swing motion energy, the RP-TENG is vertically mounted on a linear motor that simulates the repetitive movements of the arms and legs. **Figure 3a,b** presents the  $V_{OC}$  and  $I_{SC}$  of the RP-TENG at different repetition frequencies (0.5, 0.75, 1.0, 1.25, 1.5, 1.75, 2.0 Hz), respectively. We can see that as the frequency increases from 0.5 to 2.0 Hz, the  $V_{OC}$  first increases then remains steady. At the frequency of 0.5 Hz, the amplitude  $\theta < 1.5^\circ$ , i.e., the relative motion between the rotor and stator is small, thus results in a relatively peak value of the  $V_{OC}$ . As the frequencies increases (0.75 Hz), the amplitude  $\theta$  becomes larger, so is the peak value of the  $V_{OC}$ ; once the  $\theta$  is larger than  $1.5^\circ$  (1.0–2.0 Hz), the  $V_{OC}$  reaches its maximum and remains steady. While for the  $I_{SC}$ , the output peaks at the resonance frequency of 1.5 Hz. The  $V_{OC}$  and  $I_{SC}$  at the frequency of 1.5 Hz are  $83.6 \pm 0.5$  and  $8.46 \pm 0.08 \mu A$ , respectively. To obtain the maximum output power, the electrical output of the RP-TENG was measured at the frequency of 1.5 Hz using resistors as external loads. As shown in Figure 3c, it is clear that as the load resistance increases, the peak value of the  $I_{SC}$  drops due to the Ohmic loss, and the maximum instantaneous peak power ( $P = I^2 R$ ) is 0.29 mW at a load resistance of 10 M $\Omega$ . The corresponding maximum instantaneous power density is 35.2 mW m<sup>-2</sup>. The charging behavior of the RP-TENG for different capacitors is also evaluated. The voltage curve of the 22, 47, 100, and 470 nF capacitors charged by the RP-TENG at the

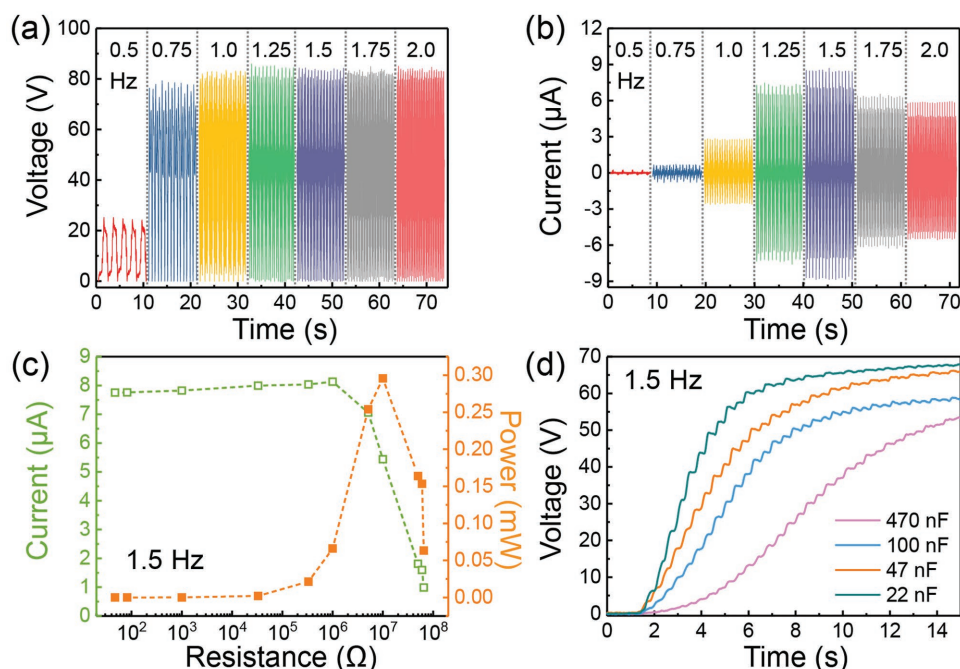


**Figure 3.** a) Open-circuit voltage ( $V_{OC}$ ) of the RP-TENG at different repetition frequencies. b) Short-circuit current ( $I_{SC}$ ) of the RP-TENG at different repetition frequencies. c) Output current and power under variable load resistance at the repetition frequency of 1.5 Hz. d) The measured voltage curve of the 22, 47, 100, and 470 nF capacitors charged by the RP-TENG at the repetition frequency of 1.5 Hz.

frequency of 1.5 Hz is shown in Figure 3d. In 10 s, the 22, 47, 100, 470 nF capacitor can be charged from 0 to 66.4, 63.6, 56.2, and 43.1 V, respectively. These results indicate that the RP-TENG is capable of harvesting energy from human walking.

Except for the regular movement of human motion, the RP-TENG is also able to harvest energy from acceleration or deceleration processes. Figure 4a indicates the  $I_{SC}$  of the RP-TENG at different accelerations. The acceleration is precisely controlled by the linear motor, where the RP-TENG is vertically mounted. The acceleration used ranges from 1 to 25  $m\ s^{-2}$  with a step of 2  $m\ s^{-2}$ . As the vertical-aligned RP-TENG accelerated leftward, the rotor swayed toward the right side with respect to the stator, hence an electrical current was produced. It can be seen that as the acceleration increases from 1 to 21  $m\ s^{-2}$ , the peak value of the current increase from 1.12 to 8.32  $\mu A$ . With further increase in acceleration, the peak value remains steady. The relationship between current amplitude and acceleration is plotted in Figure 4b. We can see that in the range of 1–21  $m\ s^{-2}$ , a linear relationship can be derived. The good linearity also indicates the capability of the RP-TENG as an acceleration sensor, which has a detection range of 1–21  $m\ s^{-2}$  and a sensitivity of  $0.335 \pm 0.008\ \mu A\ s^2\ m^{-1}$ .

One major advantage of the pendulum structure is its sensitivity to minor changes from the vertical level. As for the vertically placed RP-TENG, the changes from the vertical level will result in a relative motion between the rotor and stator, hence induces a potential difference between Electrode A and Electrode B. In order to evaluate the sensitivity of the RP-TENG, the  $V_{OC}$  generated by the RP-TENG at a small tilt angle ranging from 0.25 to 1.35 are shown in Figure 4c. The tilt angle is measured by a digital protractor, and at the angle of 0°, the bisectors

of the rotor and stator are paralleled to the direction of gravity. It can be seen that the  $V_{OC}$  measured at the angle of 0.25°, which is the lowest detection limit, is 0.70 V. In the range of 0.35° and 1.15°, the  $V_{OC}$  linearly increases from 0.73 to 19.9 V as the tilt angle increases and the linear fit gives a sensitivity of  $24.0 \pm 0.6\ V\ s^2\ m^{-1}$ . Therefore, any small mechanical agitation that causes the tilt or vibration can be detected by the RP-TENG. Compared with the tilt sensor based on magnetic-assisted triboelectric nanogenerators,<sup>[27]</sup> which is insensitive to the tilt angle less than 30°, the RP-TENG with a lower detection limit of 0.25° has a higher sensitivity owing to its radial-grating structure.

Figure 5 demonstrates the capability of the RP-TENG for energy harvesting and tilting-angle sensing. In Figure 5a,b, the RP-TENG is attached to the lower leg of a person and the basket of a bicycle, respectively, in order to harvest the energy of the legs during walking and the energy of the bicycle in the deceleration processes. In both cases, 18 commercial light-emitting diodes (LEDs) can be instantaneously driven through a bridge rectifier (Video S1, part 1 and part 3, Supporting Information). The inset of Figure 5a shows the illuminating LEDs after the person stops walking, where the rotor continues to oscillate for another several cycles before it comes to rest (Video S1, part 2, Supporting Information). Since the tilt motion will induces a relative motion between the rotor and stator, the RP-TENG can also be utilized to harvest energy from the tilt motions, such as constant water wave motions. Thus, the scalability of the RP-TENG is of crucial importance for large-scale applications, where the RP-TENGs are connected so that they are in synchronized motion (see Figure 5c). To prove its scalability, up to four pairs of triboelectric layers are parallel-connected. The measurements were also taken by releasing the rotor from its

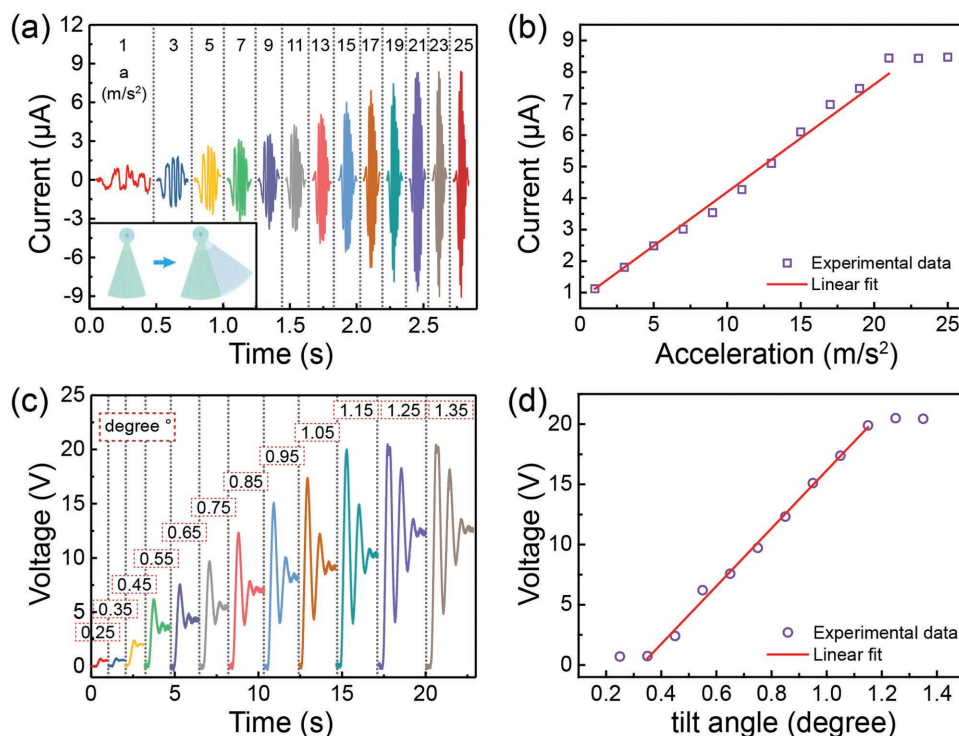


**Figure 4.** a) Short-circuit current ( $I_{SC}$ ) of the RP-TENG when the acceleration increases from 1 to 25  $m s^{-2}$  with a step of 2  $m s^{-2}$ . b) Relationship between current amplitude and acceleration. c) Open-circuit voltage ( $V_{OC}$ ) of the RP-TENG at different tilt angles. d) Relationship between voltage amplitude and tilt angle.

maximum displacement angle  $\theta_{max}$ . We can see in Figure 5d that the  $I_{SC}$  produced in the first half-cycle by one pair of the triboelectric layers is 4.45  $\mu A$ ; while by four pairs the output current can be increased up to 12.83  $\mu A$ , which is 2.9 times as large as that of one pair. The increment is attributed to the larger contact area between the triboelectric layers, hence a larger amount of triboelectric charges. Therefore, the RP-TENG may become a potential candidate for large-scale blue-energy harvesting.<sup>[2,28]</sup>

As presented in Figure 4c,d, the high sensitivity of the RP-TENG makes it an ideal system for detecting rapid motions due to external accelerations, vibrations, or tilt of the ground or structures. Based on the open source Arduino platform of an Arduino-based board and an integrated development environment, we developed a RP-TENG integrated tilt sensing alarm system. The system consists of the RP-TENG as tilt sensor and an Arduino-based power management circuit. Figure 5e presents the circuit diagram of the power management circuit. A red LED and a piezo speaker, which are triggered by the potential difference between Electrode A and Electrode B, are used as the indicators for the tilt event of the system. Figure 5f,g shows the photographs of the power management circuit and the RP-TENG integrated tilt sensing alarm system, respectively. As demonstrated in Figure 5h, when the RP-TENG is at rest, there is no potential difference between Electrode A and Electrode B, hence the system is not activated. Once the system is tilted by external agitations, the relative motion between the rotor and stator created a potential difference, i.e., a voltage signal, that activated the alarm system, so that the red LED blink and the piezo speaker

beeps. Therefore, the RP-TENG integrated tilt sensing alarm system can be applied in security systems, or to monitor seismic activities, such as earthquake and volcanic eruption.

### 3. Conclusion

In conclusion, we demonstrate a RP-TENG for energy harvesting and tilting-angle sensing. Employing the pendulum structure, the RP-TENG has been applied to capture biomechanical energy from human motion or harness the energy in acceleration or deceleration processes of moving vehicles. The electrical performance of the RP-TENG is systematically studied by using a linear motor to simulate the repetitive movements of the arms and legs during walking at the repetition frequency of 0.5, 0.75, 1.0, 1.25, 1.5, 1.75, and 2.0 Hz. At the resonance frequency of 1.5 Hz, the  $V_{OC}$  and  $I_{SC}$  produced are  $83.6 \pm 0.5$  and  $8.46 \pm 0.08$   $\mu A$ , respectively, and the maximum instantaneous power density is 35.2  $mW m^{-2}$  at a load resistance of 10  $M\Omega$ . Through parallel-connecting four pairs of triboelectric layers, the  $I_{SC}$  can be increased from 4.45  $\mu A$  for one pair of triboelectric layers to 12.83  $\mu A$ , which is 2.9 times as large as that of one pair, thus making it a potential candidate for harvesting large-scale blue-energy. Furthermore, the RP-TENG has a high sensitivity to minor changes from the vertical level. Owing to its radial-grating structure, the lower detection limit of the RP-TENG is 0.25°, and a RP-TENG integrated tilt sensing alarm system is developed, which can be applied in security or seismic monitoring systems.

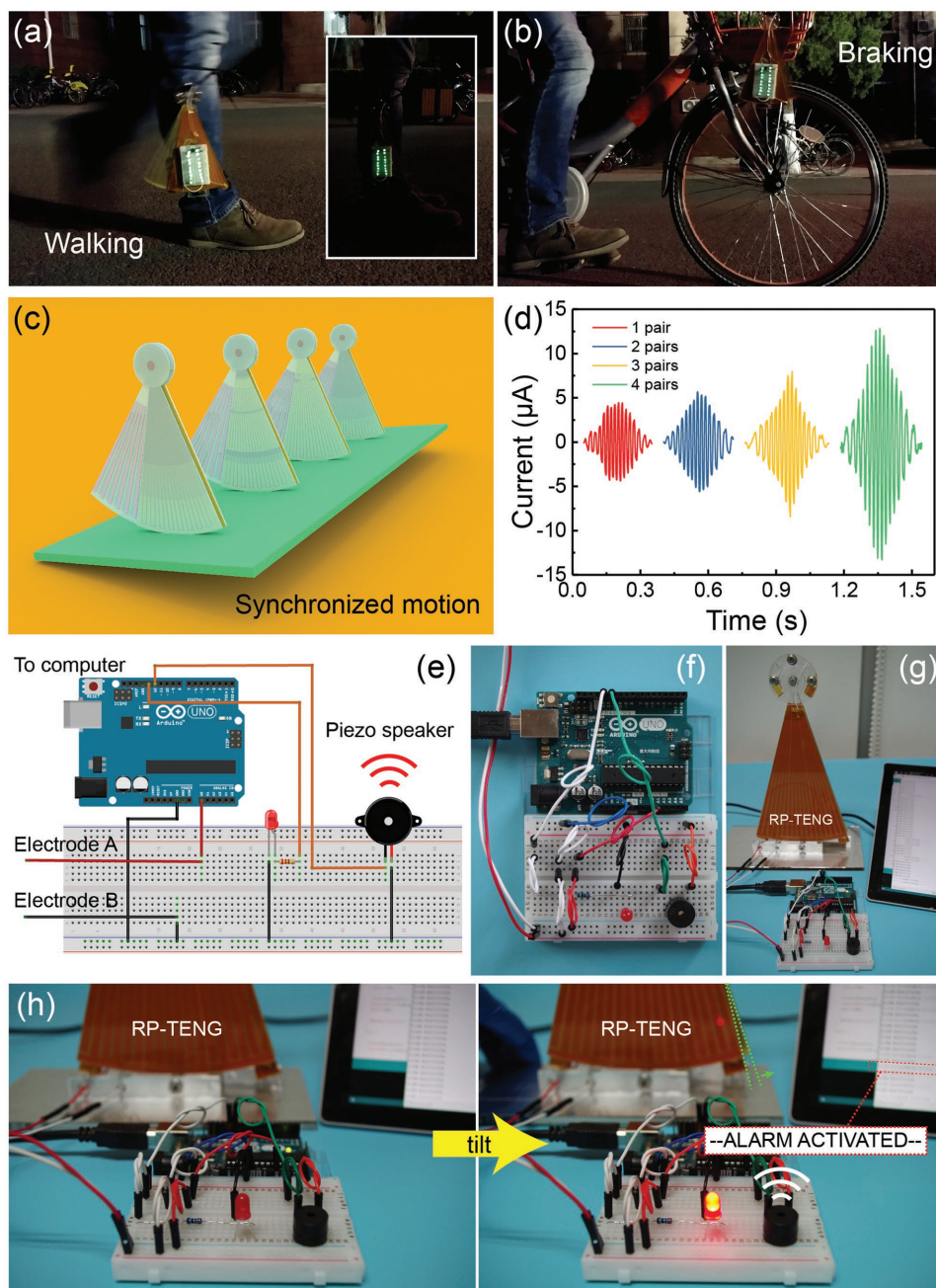


**Figure 5.** a) Demonstration of the PR-TENG for harvesting biomechanical energy from human walking. b) Demonstration of the RP-TENG for harvesting energy in the deceleration process of the braking. c) Demonstration of the parallel-connected RP-TENGs for tilt motions. d) Short-circuit current ( $I_{SC}$ ) produced in the first half-cycle by different pairs of the triboelectric layers. e) Diagram of the power management circuit. f,g) Photograph of the power management circuit and the RP-TENG integrated tilt sensing alarm system. h) Demonstration of the PR-TENG integrated tilt sensing alarm system.

## 4. Experimental Section

The RP-TENG consists of a rotor and stator that are coaxially aligned. Both the rotor and stator have a sectorial structure with a radius of 200 mm and a central angle of 36°. The rotor has three components: the acrylic substrate with a thickness of 5 mm and two pair of sectorial electrodes on both sides of the substrate. On each side, there are 18 radially aligned sectorial electrodes with a length of 143 mm and a central angle of 1.5°. The included angle between two adjacent

PTFE films is 4.1°. The stator has two identical units and on the inner surface of each unit, there are two interlocking sectorial electrodes, which has the same pattern as that of the rotor. On top of the interdigitated electrodes, there is a layer of PTFE film with a thickness of 80 μm. All the electrodes are prepared by industrial PCB technology. The electrode is made of copper and has a thickness of 35 μm, while thickness of the board is 0.40 mm. All the electrical measurements of the RP-TENG were performed using the Keithley 6514 system Electrometer.

## Supporting Information

Supporting Information is available from the Wiley Online Library or from the author.

## Acknowledgements

C.H. and B.D.C. contributed equally to this work. Supports from National Key R & D Project from Minister of Science and Technology (No. 2016YFA0202704), National Natural Science Foundation of China (Grant Nos. 51432005, 51608039, 5151101243, 51561145021, and 51608039), China Postdoctoral Science Foundation (Grant No. 2015M581041), China Postdoctoral Science Foundation (Grant No. 2015M581041), and Natural Science Foundation of Beijing, China (Grant No. 4154090) are appreciated.

## Conflict of Interest

The authors declare no conflict of interest.

## Keywords

energy harvesters, pendulum, radial grating, tilting-angle sensing, triboelectric nanogenerators

Received: September 15, 2017

Revised: January 10, 2018

Published online:

- 
- [1] Z. L. Wang, *ACS Nano* **2013**, *7*, 9533.  
 [2] Z. L. Wang, T. Jiang, L. Xu, *Nano Energy* **2017**, *39*, 9.  
 [3] F.-R. Fan, Z.-Q. Tian, Z. L. Wang, *Nano Energy* **2012**, *1*, 328.  
 [4] W. Yang, J. Chen, G. Zhu, J. Yang, P. Bai, Y. Su, Q. Jing, X. Cao, Z. L. Wang, *ACS Nano* **2013**, *7*, 11317.  
 [5] J. Chen, G. Zhu, W. Yang, Q. Jing, P. Bai, Y. Yang, T.-C. Hou, Z. L. Wang, *Adv. Mater.* **2013**, *25*, 6094.  
 [6] X. Wang, S. Niu, F. Yi, Y. Yin, C. Hao, K. Dai, Y. Zhang, Z. You, Z. L. Wang, *ACS Nano* **2017**, *11*, 1728.  
 [7] S. Niu, S. Wang, Y. Liu, Y. Zhou, L. Lin, Y. Hu, K. C. Pradel, Z. Wang, *Energy Environ. Sci.* **2014**, *7*, 2339.  
 [8] S. Wang, L. Lin, Y. Xie, Q. Jing, S. Niu, Z. L. Wang, *Nano Lett.* **2013**, *13*, 2226.  
 [9] G. Zhu, Z.-H. Lin, Q. Jing, P. Bai, C. Pan, Y. Yang, Y. Zhou, Z. L. Wang, *Nano Lett.* **2013**, *13*, 847.  
 [10] Z.-H. Lin, Y. Xie, Y. Yang, S. Wang, G. Zhu, Z. L. Wang, *ACS Nano* **2013**, *7*, 4554.  
 [11] P. Bai, G. Zhu, Z.-H. Lin, Q. Jing, J. Chen, G. Zhang, J. Ma, Z. L. Wang, *ACS Nano* **2013**, *7*, 3713.  
 [12] S. Li, J. Wang, W. Peng, L. Lin, Y. Zi, S. Wang, G. Zhang, Z. L. Wang, *Adv. Energy Mater.* **2017**, *7*, 1602832.  
 [13] W. Du, X. Han, L. Lin, M. Chen, X. Li, C. Pan, Z. L. Wang, *Adv. Energy Mater.* **2014**, *4*, 1301592.  
 [14] Q. Jing, G. Zhu, P. Bai, Y. Xie, J. Chen, R. P. S. Han, Z. L. Wang, *ACS Nano* **2014**, *8*, 3836.  
 [15] G. Zhu, J. Chen, T. Zhang, Q. Jing, Z. L. Wang, *Nat. Commun.* **2014**, *5*, 3426.  
 [16] C. Han, C. Zhang, W. Tang, X. Li, Z. L. Wang, *Nano Res.* **2015**, *8*, 722.  
 [17] Y. Xie, S. Wang, S. Niu, L. Lin, Q. Jing, J. Yang, Z. Wu, Z. L. Wang, *Adv. Mater.* **2014**, *26*, 6599.  
 [18] G. Zhu, Y. S. Zhou, P. Bai, X. S. Meng, Q. Jing, J. Chen, Z. L. Wang, *Adv. Mater.* **2014**, *26*, 3788.  
 [19] C. Bao Han, W. Du, C. Zhang, W. Tang, L. Zhang, Z. Lin Wang, *Nano Energy* **2014**, *6*, 59.  
 [20] L. Lin, Y. Xie, S. Wang, W. Wu, S. Niu, X. Wen, Z. L. Wang, *ACS Nano* **2013**, *7*, 8266.  
 [21] B. Meng, W. Tang, Z.-H. Too, X. Zhang, M. Han, W. Liu, H. Zhang, *Energy Environ. Sci.* **2013**, *6*, 3235.  
 [22] M. Ma, Z. Zhang, Q. Liao, F. Yi, L. Han, G. Zhang, S. Liu, X. Liao, Y. Zhang, *Nano Energy* **2017**, *32*, 389.  
 [23] Q. Jing, Y. Xie, G. Zhu, R. P. Han, Z. L. Wang, *Nat. Commun.* **2015**, *6*, 8031.  
 [24] Y. S. Zhou, G. Zhu, S. Niu, Y. Liu, P. Bai, Q. Jing, Z. L. Wang, *Adv. Mater.* **2014**, *26*, 1719.  
 [25] Z. L. Wang, J. Song, *Science* **2006**, *312*, 242.  
 [26] K.-E. Byun, M.-H. Lee, Y. Cho, S.-G. Nam, H.-J. Shin, S. Park, *APL Mater.* **2017**, *5*, 074107.  
 [27] M. Han, X.-S. Zhang, X. Sun, B. Meng, W. Liu, H. Zhang, *Sci. Rep.* **2014**, *4*, 4811.  
 [28] Z. L. Wang, *Nature* **2017**, *542*, 159.